

## An Automated Neural-Fuzzy Approach to Malignant Tumor Localization in 2D Ultrasonic Images of the Prostate

Samar Samir Mohamed,<sup>1</sup> J. M. Li,<sup>1</sup> M. M. A. Salama,<sup>1</sup> G. H. Freeman,<sup>1</sup> H. R. Tizhoosh,<sup>2</sup> A. Fenster,<sup>3</sup> and K. Rizkalla<sup>4</sup>

In this paper, a new neural-fuzzy approach is proposed for automated region segmentation in transrectal ultrasound images of the prostate. The goal of region segmentation is to identify suspicious regions in the prostate in order to provide decision support for the diagnosis of prostate cancer. The new automated region segmentation system uses expert knowledge as well as both textural and spatial features in the image to accomplish the segmentation. The textural information is extracted by two recurrent random pulsed neural networks trained by two sets of data (a suspicious tissues' data set and a normal tissues' data set). Spatial information is captured by the atlas-based reference approach and is represented as fuzzy membership functions. The textural and spatial features are synthesized by a fuzzy inference system, which provides a binary classification of the region to be evaluated.

**KEY WORDS:** TRUS, prostate cancer, RNN, fuzzy inference, tissue segmentation, textural feature, spatial feature, malignant tumor localization

### INTRODUCTION

Prostate cancer is the second most common type of cancer in Canadian men, and in 2010, an estimated 25,500 new cases will be diagnosed. This type of cancer is ranked third with respect to mortality, causing 4,300 deaths annually.<sup>1</sup>

Early detection means possible recovery. However, there is a huge debate on prostate cancer treatment which is a controversial subject. A review on different treatment options is explained by Heidenreich et al. in.<sup>2</sup> A prostate-specific antigen value analysis and a digital rectal examination are the methods used to detect signs of cancer during screening, after which, a prostate biopsy is performed in order to arrive at a conclusive diagnosis of the disease. However, a prostate biopsy can miss

some cancers, especially in the case of a random sextant biopsy operation.<sup>3,4</sup>

Different imaging methods such as Gray-scale, color, and power Doppler sonography were compared in.<sup>5</sup> It was concluded that Gray-scale and Doppler methods did not expose prostatic cancer with sufficient accuracy to replace sextant biopsy. It was also proven that the power Doppler method might be useful for targeted biopsies if the number of biopsy passes have to be limited.<sup>5</sup> In a more recent research, Turgut et al. assessed the role of spectral Doppler sonographic parameters of the arteries feeding the prostate gland for prostate cancer detection, and they recommended that further research is needed to elucidate the potential of spectral Doppler indices.<sup>6</sup> Moreover, Halpern et al. evaluated the value of directed biopsy for prostate cancer detection during contrast-enhanced sonography. In that research, they concluded that contrast-enhanced transrectal sonography improves the detection of malignant tumors in the prostate gland.<sup>7</sup>

---

<sup>1</sup>From the Department of Electrical and Computer Engineering, University of Waterloo, 619 Honeywood place, Waterloo, ON, Canada N2T 2T6.

<sup>2</sup>From the Department of Systems Design Engineering, University of Waterloo, Waterloo, Canada.

<sup>3</sup>From the Department of Diagnostic Radiology and Nuclear Medicine, University of Western Ontario, London, ON, Canada.

<sup>4</sup>From the Department of Pathology, University of Western Ontario, London, ON, Canada.

Correspondence to: Samar Samir Mohamed, Department of Electrical and Computer Engineering, University of Waterloo, 619 Honeywood place, Waterloo, ON, Canada N2T 2T6; tel: +1-519-7221722; fax: +1-519-7463077; e-mail: smohamed@hivolt.uwaterloo.ca

Copyright © 2010 by Society for Imaging Informatics in Medicine

Online publication 8 June 2010

doi: 10.1007/s10278-010-9301-x

From the previous discussion, it can be concluded that guiding biopsy operations without reducing the sensitivity or specificity of the diagnostic procedure is beneficial and is possible with transrectal ultrasound (TRUS) image analysis. Typically, in this procedure, a radiologist manually identifies, with a moderate degree of confidence, the suspicious regions of the prostate in the TRUS image based on the intensity, local texture, and spatial distribution of the abnormal tissue. However, the effectiveness of such a manual TRUS diagnosis is highly dependent on the experience and knowledge of the radiologist.

The goal of the research described in this paper was to design an algorithm that incorporates expert knowledge so that suspicious regions of the prostate identified in TRUS images can be segmented and diagnostic decisions that mimic those of expert radiologists can be obtained. Automated region segmentation thus improves the efficiency and effectiveness of the process for diagnosing prostate cancer, and it has the potential of reducing the number of biopsies required for accurate diagnosis. To construct an effective automated region segmentation algorithm, the features that characterize the regions of interest must be selected, following which a segmentation approach must be used in order to separate the regions according to distinguishing features.

Two classes of features are typically used for medical image segmentation: pixel-based and local neighborhood-based. The latter method is considered more suitable for use in segmentation discrimination.

An example of the manual tissue segmentation is depicted in Figure 1. The visual features of the

TRUS images that aid in manual segmentation include intensity, which is a pixel-based feature; local texture differences, which are a local neighborhood feature; and the spatial distribution of the abnormality.

Intensity is one of the discriminators that radiologists use to determine suspicious regions, and they usually identify diminished echogenic regions in the peripheral zone of the prostate as cancerous.<sup>8</sup> However, low specificity is associated with this method of localizing an abnormality.<sup>9</sup> Furthermore, 25% of prostate cancer appears in the isoechoic regions within the peripheral zone, and these cases cannot be detected by intensity-based indicators.<sup>9</sup> Therefore, the research shows few instances of the use of intensity alone for the automated localization of prostate cancer abnormalities.

Another distinguishing visual feature is the local texture of the image. The parenchyma of malignant tissues differ from those of benign tissues so that the acoustic energy is reflected and scattered differently.<sup>10</sup> Part of this difference is likely to be manifested in the TRUS images as variations in the local texture. Previous studies of the application of a local textural indicator includes work by Scheipers et al., who calculated first- and second-order co-occurrence parameters in order to express the differences in local texture.<sup>12</sup> In other research by Mohamed et al., multiresolution analysis was applied in order to segment the internal regions of the prostate, with excellent results that matched the regions identified by the radiologist.<sup>13,14</sup> Spectral clustering was also used successfully by Mohamed et al. for prostate gland segmentation.<sup>15</sup>

Statistically, 68% of prostate cancer originates in the peripheral zone, and only 24% originates in

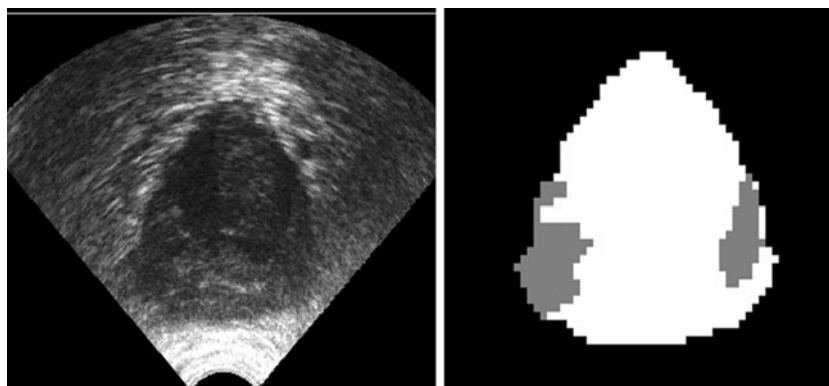


Fig. 1. The segmentation problem: original TRUS image of the prostate (*left panel*) and manual segmentation of a malignant region as performed by a radiologist (*right panel*).

the transition zone.<sup>8</sup> The peripheral and transition zones can be located spatially in TRUS images. Chen et al. examined the spatial distribution of prostate cancer.<sup>16</sup> However, the investigation of the use of the statistics of the spatial distribution as a discriminator is an approach rarely described in existing papers about the automated localization of prostate abnormalities. This paper explores the local texture properties of both suspicious and normal tissues and how textural differences can best be captured by an automated algorithm. It also examines how spatial information can be incorporated into such an algorithm.

Because local texture is one of the primary distinguishing features of the regions, the extraction of textural features to be used as input for a classifier that yields a binary decision seems a viable approach. Loch et al.<sup>17</sup> have recently explored the use of a feedforward artificial neural network (ANN) to differentiate between malignant and benign regions in TRUS images. However, in their work, the training and evaluation samples ( $18 \times 18$  pixel blocks within the image) were selected randomly from the same set of images. Therefore, whether this approach can produce generalized results for image samples which are not used in the training set is questionable.

Loch et al. used six local texture descriptors as input for the feedforward ANN, including the number of edges, the dispersion of the edge intensity, the average size of the edges, the dispersion of the edge size, the contrast intensity of the edges, and the dispersion of the edge contrast. Mohamed et al. explored a different avenue of feature construction by using spectral features in which the segmented regions were scanned to form 1D signals and different spectral features were constructed from the signals obtained.<sup>20</sup> A comprehensive classical approach to texture feature construction was demonstrated by McNitt-Gray et al.<sup>18</sup> 59 spatial and textural features were evaluated in the segmentation of chest radiographs. However, since these textural features are mostly equation-based, there can be no guarantee that they will fully capture the complex textural properties of ultrasound images. Aboul Ella Hassanien<sup>19</sup> used a blend of fuzzy logic, pulse coupled neural networks, wavelets and rough sets, for analyzing prostate TRUS images for prostate cancer diagnosis

Gelenbe's supervised recurrent random pulsed neural network (RNN) offered a more structurally

sophisticated alternative for capturing the complex textural information that is based on the recursive nature of the training of the RNN network weights.<sup>21-26</sup> The RNN is also simple to implement because it encodes textural information in the local neighborhood without explicitly extracting features.

Fuzzy inference can be used to process the results produced by spatial and textural information analyses and to provide a binary classification. Scheipers et al. used spectral and textural parameters extracted from TRUS images of the prostate region as input for building two fuzzy inference systems (FISs) with the goal of locating prostate carcinoma.<sup>12</sup> Six Gaussian membership functions were used per input parameter. One FIS was used to distinguish hypoechoic and hyperechoic tumors from normal tissue. The other FIS was used to segment isoechoic tumors from normal tissue. However, evaluating TRUS images using Scheipers' approach requires prior knowledge of the type of tumor (whether hypoechoic/hyperechoic or isoechoic). Furthermore, the two FISs they proposed require either six or seven types of input, which incurs a high computational expense. Our work applies only three parameters, each with two membership functions.

In this paper, "Outline of the System Architecture" section outlines the proposed algorithm architecture, and "Fuzzy Inference Stage" section details the implementation of the RNN. The fuzzy inference system is explained in "Results" section. The results produced by the proposed technique when it is applied to clinical TRUS images are presented in "Comparison with Other Methods" section. "Discussion" section summarizes the strengths and weaknesses of the proposed method and suggests possible future improvements. The results and additional issues are summarized in "Conclusions" section.

## OUTLINE OF THE SYSTEM ARCHITECTURE

The goal of the proposed method is to automatically segment suspicious regions in TRUS images by simulating the manual analysis of an experienced radiologist. The manually segmented ultrasound images used in the analysis for this research were obtained during clinical screening sessions using an Aloka 2000 ultrasound machine with a broadband 7 MHz linear transducer and a field of view of approximately 6 cm. Manual segmentation

was adopted as the gold standard for evaluating the degree of interoperator agreement between the manual approach and the proposed approach. Before the tissue was segmented using the new approach, the contour of the prostate was segmented using the deformable model approach.<sup>11</sup> The segmented prostate was then used as the input for training and evaluating the automated tissue segmentation system.

The new method captures the specific textural and spatial information in the TRUS images that has been identified in “Introduction” section as important for discriminating between normal and suspicious regions. Our method captures textural information using the RNN as a supervised classifier. The spatial information is incorporated into an atlas-based reference approach and is represented as fuzzy membership functions. These two features are then synthesized with a fuzzy inference system that provides a classification of the binary tissue region.

The RNN requires training based on manually segmented data. After the training is completed, the overall system is evaluated using a different set of TRUS images.

The new image segmentation system consists of the two stages shown in Figure 2. The input into the first stage includes the scaled pixel intensities of the  $5 \times 5$  input block and the  $x$ - $y$  position of the top-left pixel of the block. The first stage of the system consists of two RNN networks as well as the horizontal and vertical position finders. The RNNs are trained with data from both the normal and

suspicious regions. The horizontal and vertical position finders assign relative position labels to the input image block to be evaluated. The result of this operation is similar to image registration, in which image partitions belonging to the same anatomical regions of different images are aligned. The output of the first stage, which is used as input to the second stage, includes the difference between the output from the RNN networks and the relative position of the input block with respect to the prostate as a whole.

The second stage of the system is composed of the FIS, in which three membership functions (MFs) translate the input values from the first stage into membership values that are used in the subsequent fuzzy inferencing. MF1 refers to the RNN output difference input, and MF2 and MF3 refer to the relative horizontal and vertical position input. Fuzzy inferencing provides an output value between 0 and 1, which corresponds to the likelihood that a specific input block belongs to a suspicious region (the higher the output value, the higher the likelihood of the input block being abnormal). A threshold between 0 and 1 can be used in order to derive binary output. The components of the system are explained in detail in the following sections.

### The RNN Stage of the Algorithm

Gelenbe introduced the RNN in 1989 and used it in a variety of applications.<sup>21–26</sup> In 1996, Gelenbe et al. applied the RNN in order to segment the gray and white matter in MRI images

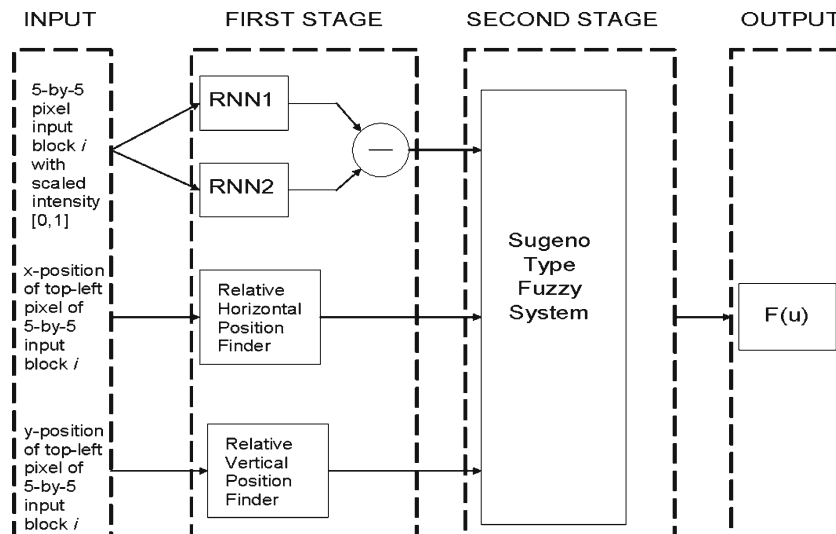


Fig. 2. System architecture.

of the brain,<sup>21</sup> thereby experimentally proving the ability of an RNN to capture textural differences between tissues in medical images. Because ultrasound images contain speckle, which is absent in MRI images and which is likely to affect the local texture in different tissue regions in a TRUS image, the performance of the RNN for segmenting ultrasound images is not as ideal as for MRI results.

If the size of the input pixel block is chosen as  $n \times n$ , each of the two RNNs is also constructed as an  $n \times n$  grid of neurons, as shown in Figure 3. Each neuron is mapped to the pixel at the same location in the  $n \times n$  grid and interacts directly only with the other neurons in the four first-order and four second-order cardinal directions (N, NE, E, SE, S, SW, W, and NW).

In the training phase, RNN1 is trained with data from the normal region, and RNN2 is trained with data from the abnormal region. The input to the RNNs consists of distinct  $5 \times 5$  blocks of pixels with each pixel having scaled intensity values between 0 and 1 (scaled from the original range of 0–255). The histogram of the input pixels is equalized with a base histogram in order to avoid large contrast variations from image to image. The base histogram is selected from one of the training images that is judged by the operator to have the maximum visual separation between the suspicious region and the normal region. The desired output of each neuron is set to be the scaled intensity of the associated pixel.

When the image blocks are evaluated, the output of each RNN is the sum of the squared errors for each block being evaluated. A sum of the squared error for one RNN that is lower than that for the other indicates that the block is more texturally similar to

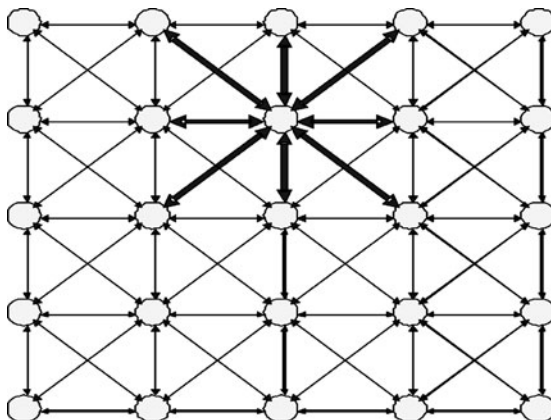


Fig. 3. RNN neuron grid, the pixel is mapped to its first and second degree neighbors (N, NE, E, SE, S, SW, W, and NW).

the region that is being used to train the lower sum RNN.

### Experimental Results of Testing the RNN Method for Segmenting Natural Textures

The RNN segmentation approach was tested by using natural texture images to address challenges such as how the output of the RNN can be appropriately post-processed in order to improve the results of the segmentation and which size of input block is optimal for capturing textural differences between regions.

The image in Figure 4 was synthesized from four sub-images, representing four distinct textures. Four RNNs were trained using each of these textures.

The segmented blocks that were produced in the evaluation phase are not connected to other segmented blocks from the same region in any of the eight first- and second-order cardinal directions and are likely the result of noise within the original image. A filter that operates in a manner similar to morphological dilation was developed and used to remove all unconnected blocks, as shown in Figure 5a. This filter was implemented at the block level, and if the label is discovered to be inconsistent with the labels of the surrounding blocks, transforms the label of that particular block. When the new filter was applied along with a median filter, a more contiguous segmentation of the four texture regions was produced, as shown in Figure 5b.

Another variable in determining the training methodology is the size of the input block. It was found that a smaller input block results in finer contours along the edges of the regions. However, more noise is created in the interior of the regions. The results from  $4 \times 4$  and  $5 \times 5$  input blocks are contrasted in Figure 6.

The post-processing procedure described in this section was followed for the evaluation of the TRUS images. For a more contiguous segmentation result, a  $5 \times 5$  input block size was selected for training the RNNs to evaluate the TRUS images.

### FUZZY INFERENCE STAGE

The fuzzy inference stage defines the relationships between the output of the RNN, the spatial distribution of the cancerous tissues in the prostate, and the desired result.

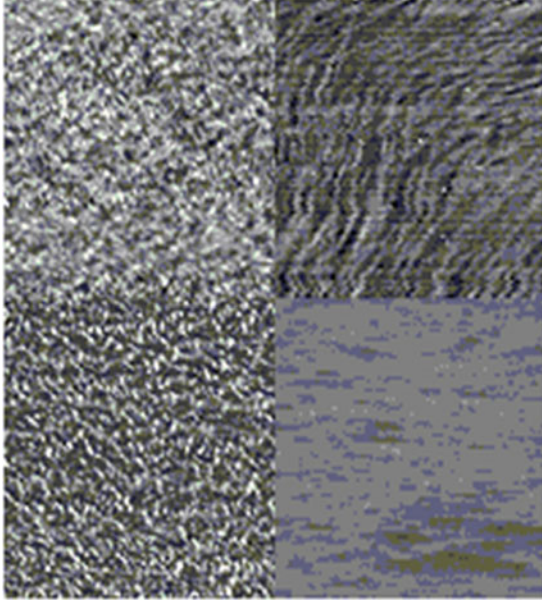


Fig. 4. Synthetic image consisting of four natural textures.

### Fuzzy Inference System

To construct the fuzzy inference system,<sup>27,28</sup> the fuzzy membership function that is associated with each of the input variables must be found. An error output from one RNN that is lower than that from the other indicates that the input block is more likely to belong to the region represented by the RNN with the lower error output. Therefore, the difference between the output values of the RNNs can be used as an indicator for classifying the input block. The amount by which the RNN output differs from the training sample ranges from  $-0.6$  to  $0.2$ . The desired results, with respect to the differences between the RNN output values, are plotted in Figure 7.

To construct the membership function, these differences are slotted into 20 uneven-sized bins, as indicated along the RNN output difference axis in Figure 7a. The bin size is chosen to be proportional to the density of the distribution of the RNN output differences, which expresses the rapid variation in the degree of membership around the RNN output difference of zero, where the distribution density is the highest. The degree of membership is obtained by dividing the number of suspicious samples by the number of total samples in that bin, as illustrated in Figure 7b. The rescaled degree of membership distribution is constructed by converting the  $x$ -axis from the uneven-sized bins back to the original RNN output difference scale. This distribution is reflected in Figure 7c, with the  $x$ -axis representing the RNN

output differences and the  $y$ -axis representing the proportion of suspicious blocks to total blocks in each RNN output difference segment. This distribution is used as the membership function  $\mu_{A_1}$ , which denotes *is abnormal*, as expressed by the RNN indicator. Its complement is used as the membership function  $\mu_{A_2}$ , which denotes *is normal*, as expressed by the RNN indicator.

The relative horizontal and vertical position finders translate the absolute pixel positions into relative positions with respect to the center of mass of the prostate in both horizontal and vertical directions. The center of mass calculation is expressed as follows:

$$CM_x = \frac{1}{N} \sum_{i=1}^N x_i \quad (1)$$

$$CM_y = \frac{1}{M} \sum_{i=1}^M y_i$$

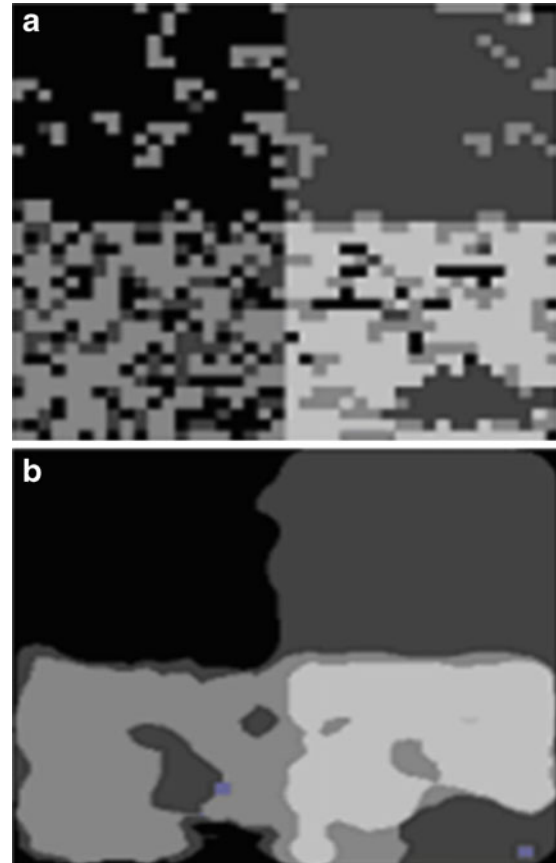


Fig. 5. Results of the RNN a after filtering out the unconnected blocks and b after the results from a were subjected to median filtering.

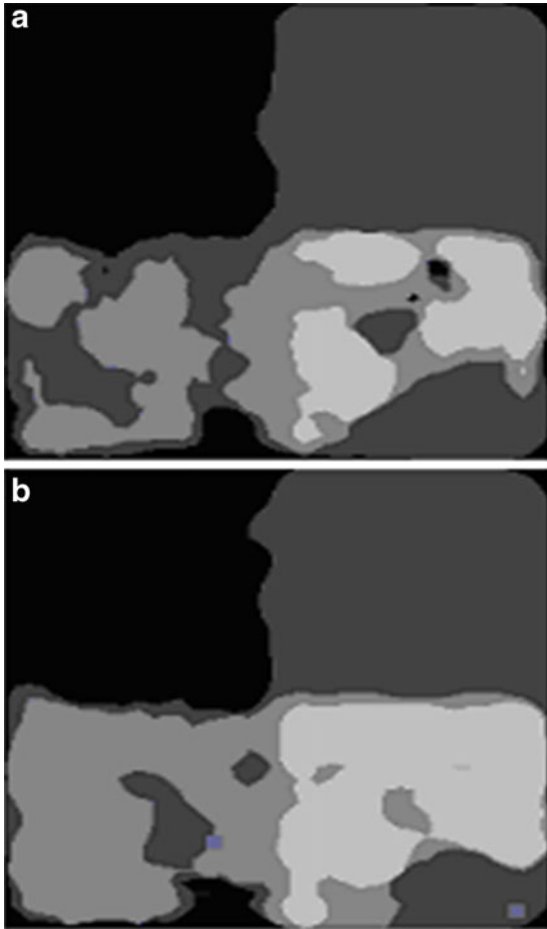


Fig. 6. Effect of the size of the input block: a results from 4×4 input blocks and b results from 5×5 input blocks.

where  $x_i$  and  $y_i$  represent the  $x$ - $y$  coordinates of the first pixel of image block  $I$ , and  $N$  and  $M$  are the total number of blocks within the prostate boundary in the  $x$  and  $y$  directions, respectively.

The relative positions in the horizontal and vertical directions are divided into 20 bins. For the horizontal distribution, bins  $-10$  to  $0$  represent the relative positions that extend from the block at the extreme left of the center of mass, and bins  $0$  to  $10$  represent the relative positions that extend from the center of mass to the block at the extreme right. Similarly, for the vertical distribution, bins  $-10$  to  $0$  represent the relative positions that extend from the block at the extreme top to the center of mass, and bins  $0$  to  $10$  represent the relative positions that extend from the center of mass to the block at the extreme bottom. The spatial distribution of the malignant tissues (the percentage of the malignant tissue blocks over the total number

of blocks in each of the relative position bins) in both directions is shown in Figure 8.

The membership function  $\mu_{B_1}$  signifies *is malignant* based on the horizontal distribution, and its complement  $\mu_{B_2}$  denotes *is benign* based on the horizontal distribution. Similarly, the membership function  $\mu_{C_1}$  represents *is malignant* based on the vertical distribution, and its complement  $\mu_{C_2}$  denotes *is benign* based on the vertical distribution. These functions are displayed in Figure 8.

The output membership functions are defined as two triangular membership functions.  $\mu_{D_1}$  represents *is benign*, and  $\mu_{D_2}$  represents *is malignant*, as illustrated in Figure 9.

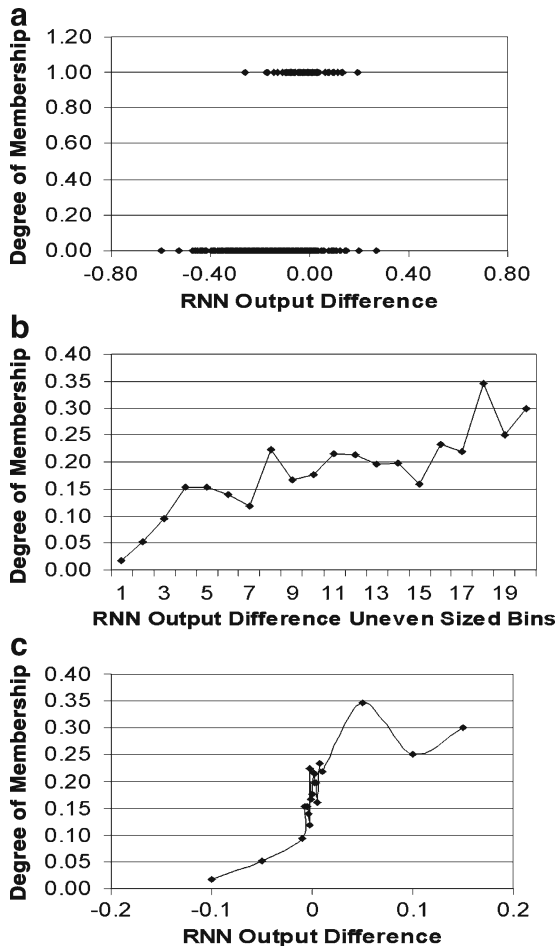


Fig. 7. Desired output with respect to a the distribution of the differences in RNN output (on  $y$ -axis,  $1$  signifies suspicious and  $0$  signifies normal), b the degree to which membership distribution is slotted into uneven-sized bins, and c the rescaled degree of membership distribution.

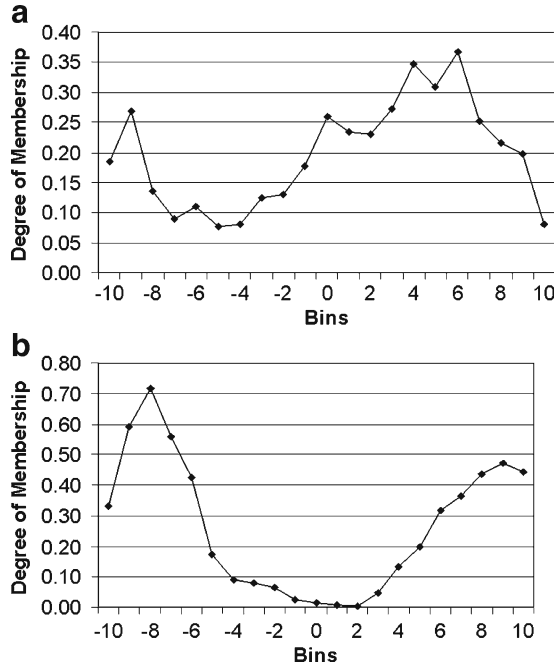


Fig. 8. Degree of membership (malignant) of input blocks in the a horizontal direction and b vertical direction.

There are 16 possible fuzzy rules. Two rules were selected based on heuristic knowledge and are represented as follows:

$R_1$ : IF  $\mu_{A_1}$  (*is malignant* from RNN output) and  $\mu_{B_1}$  (*is malignant* from horizontal distribution) and  $\mu_{C_1}$  (*is malignant* from vertical distribution),

THEN  $\mu_{D_2}$  (*is malignant*).

$R_2$ : If  $\mu_{A_2}$  (*is benign* from RNN output) and  $\mu_{B_2}$  (*is benign* from horizontal distribution) and  $\mu_{C_2}$  (*is benign* from vertical distribution), then  $\mu_{D_1}$  (*is benign*).

ELSE  
provide warning to user.

Here, when the else statement is encountered, the else action causes a warning statement to be displayed so that the user is aware of potential unintended erroneous results produced by the system.

Using the max-product inference leads to the following output:

$$D' = (A'_1 \times B'_1 \times C'_1 \circ R_1) \cup (A'_2 \times B'_2 \times C'_2 \circ R_2) \quad (2)$$

where

$$A'_1 \times B'_1 \times C'_1 \circ R_1 = \bigvee_{v,x,y} [\mu_{A_1'}(v) \wedge \mu_{B_1'}(x) \wedge \mu_{C_1'}(y)] \cdot [\mu_{A_1}(v) \cdot \mu_{B_1}(x) \cdot \mu_{C_1}(y) \cdot \mu_{D_1}(z)]$$

and

$$A'_2 \times B'_2 \times C'_2 \circ R_2 = \bigvee_{v,x,y} [\mu_{A_2'}(v) \wedge \mu_{B_2'}(x) \wedge \mu_{C_2'}(y)] \cdot [\mu_{A_2}(v) \mu_{B_2}(x) \cdot \mu_{C_2}(y) \cdot \mu_{D_2}(z)]$$

## RESULTS

Six TRUS images that consist of 7,603  $5 \times 5$  samples were used to train the RNNs. The segmentation performance of the proposed algorithm was evaluated using five TRUS images that are distinct from the training images. Based on these images, a total of 6,423  $5 \times 5$  samples were then evaluated and classified.

The receiver operating characteristic curve (ROC) analysis displayed in Figure 10 demonstrates the performance of the first-stage RNN with respect to sensitivity and specificity and of the second-stage FIS (Fig. 2) for all operating conditions. The ROC curves were obtained by continuously varying the two separation thresholds.<sup>29</sup> The separation threshold of the first-stage RNN was set as a constant for the distribution plot of the differences in the RNN output values shown in Figure 7. The area under the ROC curve (AUC)<sup>30</sup> in Figure 10 summarizes the accuracy of the test, taking into account both sensitivity and specificity

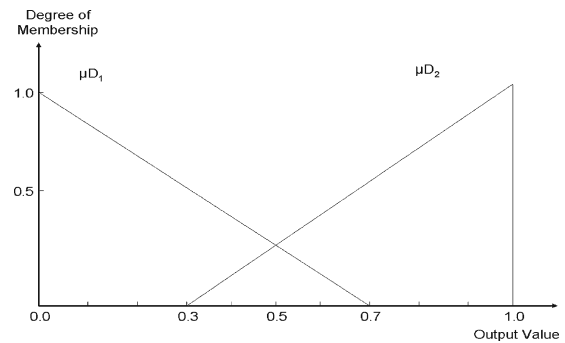


Fig. 9. Output membership functions  $\mu_{D_1}$  and  $\mu_{D_2}$ .

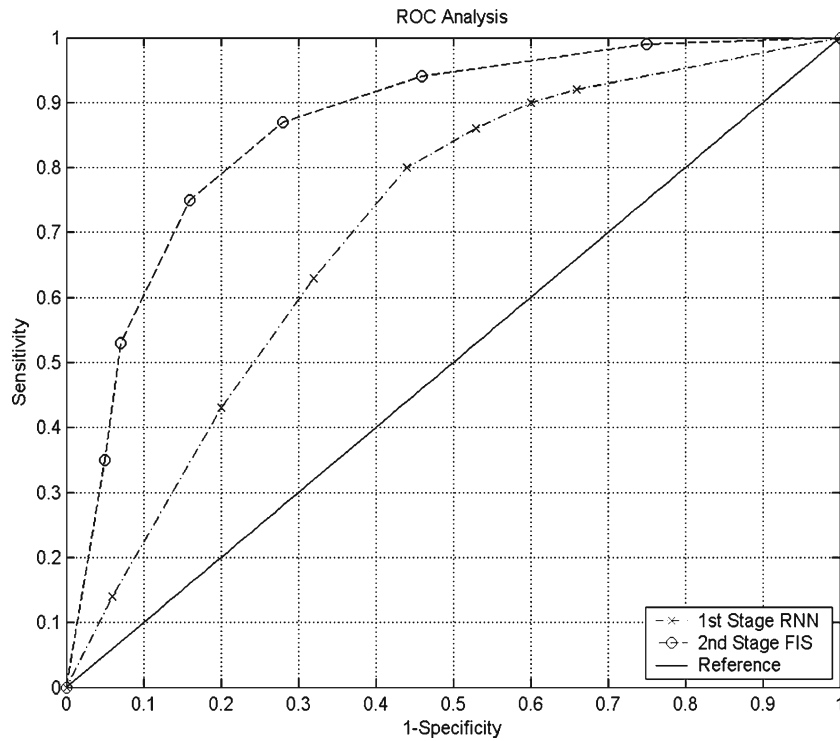


Fig. 10. ROC analysis of segmentation results.

as well as the full range of possible operating conditions. The classification rate (CR), sensitivity, and specificity are defined as follows:

$$CR = \frac{tp + tn}{tp + fn + fp + tn} \quad (3)$$

$$sensitivity = \frac{tp}{tp + fn} \quad (4)$$

$$specificity = \frac{tn}{fp + tn} \quad (5)$$

where tp denotes the true positives (the malignant blocks identified by the radiologist as correctly detected), fn denotes the false negatives (the malignant blocks that are undetected), fp denotes the false positives (the benign blocks that are wrongly detected as malignant), and tn denotes the true negatives (the benign blocks that are correctly classified as malignant). The AUC representing the first-stage RNN and the second-stage FIS are  $A_{z1} =$

0.78 and  $A_{z2} = 0.87$ , respectively. The likelihood ratio, commonly used to measure the performance of medical diagnostic tests, is proportional to tangents of the ROC curve.<sup>32</sup> The positive likelihood ratio (LR+) is defined as follows:

$$LR+ = \frac{sensitivity}{1 - specificity} \quad (6)$$

The maximum likelihood ratios represent another measure of the diagnostic performance of the three approaches. The AUC and the maximum positive likelihood ratios are listed in Table 1.

The shapes of the ROC curves indicate that the first-stage RNN approach favors high sensitivity output, whereas the FIS approach provides results with relatively high specificity. As an example, the results of the first-stage RNN and the second-stage

Table 1. Diagnostic Performance of the First-Stage RNN and the Second-Stage FIS

	AUC	Max. LR+
First-stage RNN	0.78	2.33
Second-stage FIS	0.87	7.57

FIS approaches obtained by setting the RNN output difference threshold at 0 (Fig. 7c) and the FIS output threshold at 0.22 (Fig. 9) are displayed in Figure 11.

At the RNN output difference threshold of 0, the first-stage RNN approach provides a sufficiently accurate segmentation for some cases (A, D, and

E). For all images evaluated, the first-stage RNN correctly detected 1,553 of the 1,966 samples labeled as suspicious by the radiologist, resulting in a relatively high sensitivity of 79%. However, the first-stage RNN is also prone to classifying normal regions as suspicious, correctly classifying

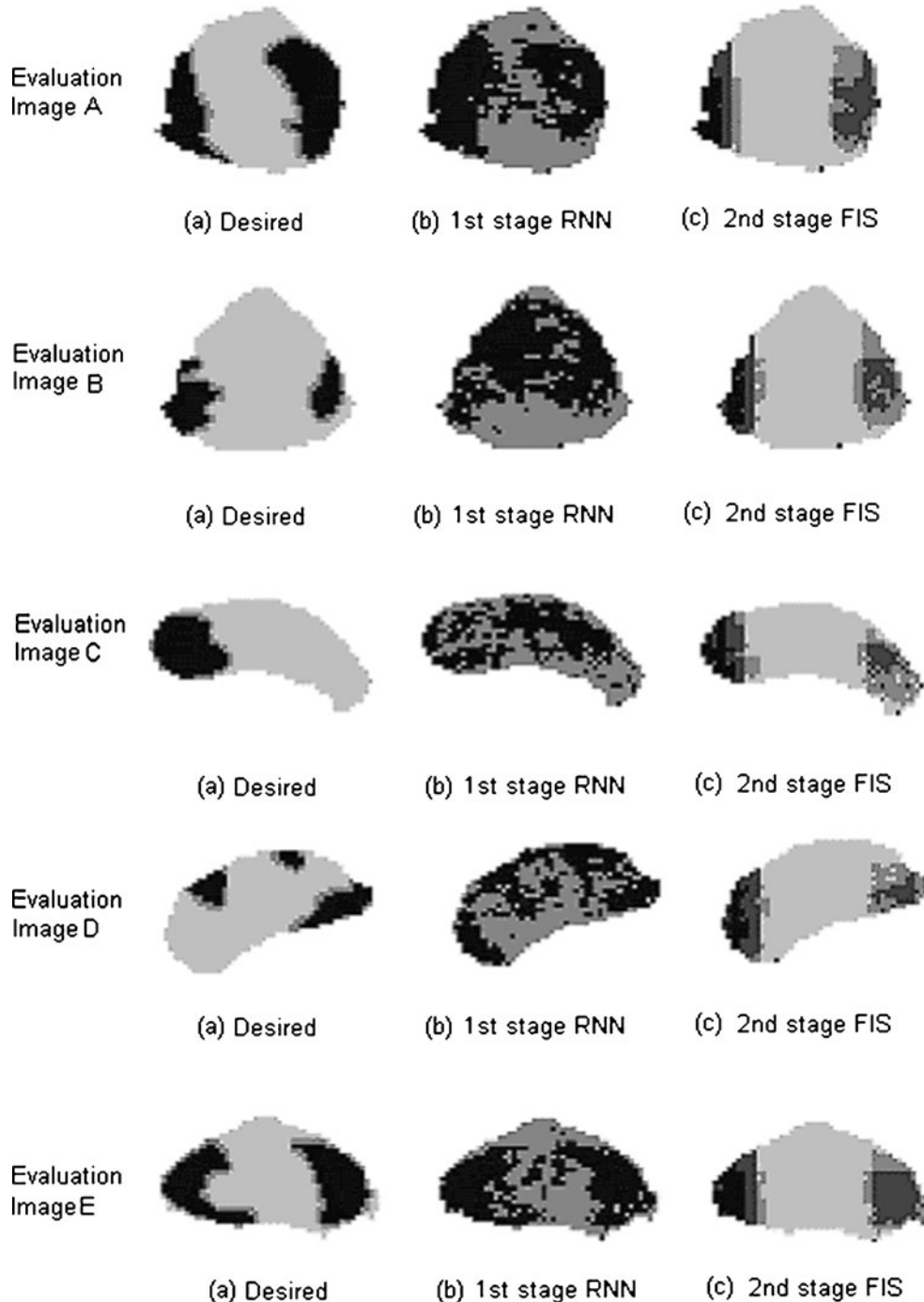


Fig. 11. Segmentation results produced by the proposed algorithm for predefined thresholds.

**Table 2. Classification Results for the First-Stage RNN and Second-Stage FIS at Thresholds of 0 (RNN Output Difference) and 0.22 (FIS Output)**

	Classification rate (%)	Sensitivity (%)	Specificity (%)
First-stage RNN	63	79	56
Second-stage FIS	81	75	84

only 2,494 of 4,457 (56%) of the samples labeled as benign by the radiologist.

At the output threshold of 0.22, the second-stage FIS classification demonstrates a high correlation with the manual segmentation, correctly identifying 5,203 of 6,423 (81%) of the labels, including 3,744 of 4,457 (84%) samples correctly predicted to be normal. Cases C and D are exceptions because the tissue classification in these two images does not correlate well with the manual segmentation. In these two images, the spatial distribution of suspicious tissue in the prostate differs significantly from that in the training set.

Table 2 summarizes the results obtained using the above thresholds with respect to the classification rate, sensitivity, and specificity of the output from each of the two stages.

COMPARISON WITH OTHER METHODS

The authors compared the results obtained by the new method to an earlier Gabor-based method<sup>13</sup>. The Gabor-based method described

in<sup>13,14</sup> was selected for the comparison because it depends on multiresolution analysis, which is an excellent method of texture segmentation. The Gabor-based ROI segmentation algorithm is able to segment the image according to the frequency response of the image, and it was chosen for this application because of its high localization in both the spatial frequency domain and the spatial domain. In addition, the ROI identification algorithm selected for this research also observes the regions selected by the expert radiologist and integrates their properties into the algorithm, which is explained in detail in.<sup>11</sup>

Examples of TRUS images A, B, and C with the regions marked by the experts are shown in part (a) of Figure 12. The candidate regions obtained using the ROI identification algorithm are shown in part (b) of the same figure. Part (c) of each of the figure shows the regions selected after the expert information is incorporated. The figures demonstrate that the Gabor-based ROI identification algorithm’s results matched to a large extent the results shown in Figure 11, which were obtained using the proposed algorithm.

DISCUSSION

This research has investigated the use of textural and spatial information to segment malignant and benign regions of TRUS images of the prostate. The results of the tests using the first-stage RNN indicate that tissue differences are manifested as

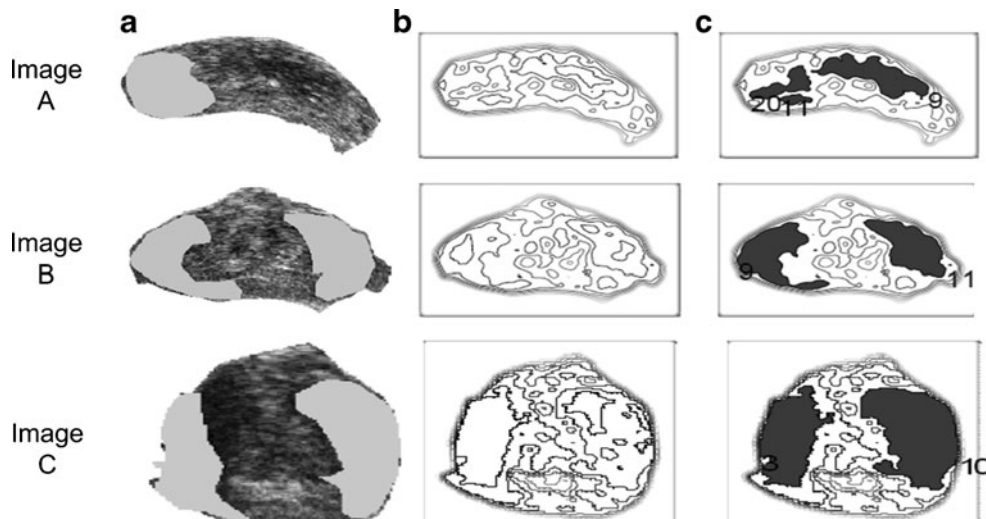


**Fig. 12. Suspicious regions for sample images A, B, and C, identified by the Gabor-based algorithm.**

local texture variations in TRUS images, which can be captured by the RNN. The results also demonstrate that the spatial distribution of the malignancy can be incorporated into the segmentation system by using a fuzzy approach that improves the specificity and the overall classification rate.

In a clinical setting, the separation thresholds should be chosen according to criteria such as mortality, discomfort to the patient, and the expense associated with the treatment or nontreatment of the disease.<sup>21</sup> If the cost of missing a positive case is deemed to be high, the operator should adjust the thresholds toward the left side of the ROC, where the sensitivity is high.

The disadvantage of using the malignant tissue distribution statistics is that the sensitivity of the second-stage classifications is poor for abnormal cases, in which the location of the malignancy differs considerably from the normal distribution. Therefore, a system that can run two parallel segmentation algorithms, one configured for high sensitivity and one for high specificity, may be more appropriate in clinical diagnostic situations.

The fuzzy inference in the proposed system applies two simple rules based on heuristic knowledge. If more were known about the causality between the input features and the likelihood of malignancy, more rules could be incorporated into the system in order to improve its performance. Furthermore, since the overlap between the output membership functions  $\mu_{D_1}$  and  $\mu_{D_2}$  (Fig. 9) is less than 50%, it may be beneficial to add a third triangular membership function  $\mu_{D_3}$ , centered around the output value of 0.5. In cases in which the input features present conflicting information, the  $\mu_{D_3}$  function could be used to address this ambiguity.

Manual localization of malignant tumors in TRUS images by a trained radiologist has a relatively moderate level of sensitivity and low specificity compared to those obtained from a sextant prostate biopsy. In this work, we have shown that an automated region segmentation system can be designed to incorporate expert knowledge and to provide segmentation results that closely approximate those obtained by an experienced radiologist. However, since manual segmentations are used to train the RNNs and to construct the spatial malignancy distribution, the clinical performance of the automated system is

upper bounded by the limited accuracy of the manual segmentation training sets.

The quality of the results obtained using the proposed method was highlighted through a comparison of these results with the ROIs obtained using the Gabor-based method: the two methods exhibit a high degree of agreement. Since TRUS image acquisition is cheaper and less invasive than sextant prostate biopsies, the proposed system has the potential to be an important supplementary tool for obtaining conclusive prostate cancer diagnoses.

## CONCLUSIONS

Segmentation of the malignant and benign regions in TRUS images is difficult due to the inherent noise in and low resolution of such images. The neural-fuzzy approach proposed in this paper uses RNNs to capture local texture differences between two tissues, a spatial atlas to incorporate the statistical information about the malignancy distribution, and fuzzy inference to synthesize the two input features in order to localize the malignant tumor.

The results obtained from the proposed automated malignant tumor localization system compare favorably with those produced by currently available automated methods. As well, the proposed system provides an additional prediction of malignancy. The output from the first-stage RNN gives the most sensitive prediction, which is enhanced by the more conservative prediction derived from the output of the second-stage FIS. The result is an improved overall level of classification accuracy.

## REFERENCES

1. National Cancer Institute of Canada. Canadian cancer statistics 2008. Toronto, Canada, 2009
2. Heidenreich A, Bolla M, Joniau S, van der Kwast TH, Matveev V, Mason, Mottet N, Schmid H-P, Wiegel T, Zattoni F. Guidelines on Prostate Cancer. *Eur Urol* 53(1):68–80, 2008
3. Presti Jr, JC, Chang JJ, Bhargava V, Shinohara K: The optimal systematic prostate biopsy scheme should include 8 rather than 6 biopsies: results of a prospective clinical trial. *J Urol* 163(1):163–167, 2000
4. Presti Jr, JC, O'Dowd GJ, Miller MC, Mattu R, Veltri RW: Extended peripheral zone biopsy schemes increase cancer detection rates and minimize variance in prostate specific antigen and age related cancer rates: results of a community multi-practice study. *J Urol* 169(1):125–129, 2003

5. Ethan J. Halpern, Stephen E. Strup. Using gray-scale and color and power doppler sonography to detect prostatic cancer. *Am J Roentgenol* 174:623–627, 2000
6. Turgut AT, Olcucuoglu E, Kosar P, Geyik PO, Kosar U, Dogra V: Power doppler ultrasonography of the feeding arteries of the prostate gland: a novel approach to the diagnosis of prostate cancer. *J Ultrasound Med* 26(7):875–883, 2007
7. Halpern EJ, Frauscher F, Rosenberg M, Gomella LG: Directed biopsy during contrast-enhanced sonography of the prostate. *Am J Roentgenol* 178(4):915–919, 2002
8. Schwartz L: Imaging and prostate cancer. *J Radiation Oncology* 36(1-supplement):118, 1996
9. Clements R: Has ultrasonography a role for screening for prostatic cancer? *Eur Radiol* 7:217–223, 1997
10. Bushberg JT, Seibert JA, Leidholdt Jr, EM, Boone JM: The essential physics of medical imaging, 2nd edition. Lippincott, Williams & Wilkins, Philadelphia, 2002, pp 469–553
11. Chiu B, Freeman GH, Salama MMA, Fenster A: Prostate segmentation algorithm using dyadic wavelet transform and discrete dynamic contour. *Phys Med Biol* 49(21):4943–4960, 2004
12. Scheipers U, Erment H, Sommerfeld H-J, Garcia-Schurmann M, Senge T, Philippou S: Ultrasonic multifeature tissue characterization for prostate diagnostics. *Ultrasound Med Biol* 29(8):1137–1149, 2003
13. Mohamed SS, Salama MMA, Kamel M, El-Sadaany EF, Rizkalla K, Chin J: Prostate cancer multi-feature analysis using TRUS images. *Phys Med Biol* 50(15):N175–N185, 2005
14. Mohamed SS, Li J, Salama MMA, Freeman G: Prostate tissue texture feature extraction for suspicious regions identification on TRUS images. *J Digit Imaging* 22(5):503–518 (doi 10.1007/s10278-008-9124-1), 2009.
15. Mohamed SS, Salama MMA: Spectral clustering for TRUS images. in *BioMedical Engineering OnLine*, 2007, 6:10 (15 March 2007)
16. Chen ME, Johnston DA, Tang K, Babaian RJ, Troncoso P: Detailed mapping of prostate carcinoma foci. *Cancer* 89(8):1800–1809, 2000
17. Loch T, Leuschner I, Genberg C, Weichert-Jacobsen K, Kuppers F, Retz M, Lehmann J, Yfantis E, Evans M, Tsarev V, Stockle M: Future trends in transrectal ultrasound. *Artificial Neural Network Analysis (ANNA) in the detection and staging of prostate cancer. Der Urologe A* 39(4):341–347, 2000
18. McNitt-Gray MF, Huang HK, Sayre JW: Feature selection in the pattern classification problem of digital chest radiograph segmentation. *IEEE Trans Med Imaging* 14:537–547, 1995
19. Hassanien Aboul Ella: Intelligence techniques for prostate ultrasound image analysis. *International Journal of Hybrid Intelligent Systems* 6(3):155–167, 2009
20. Mohamed SS, Salama MMA: Prostate cancer spectral multi-feature analysis using TRUS images. *IEEE Trans Med Imag* 27(4):548–556, 2008
21. Gelenbe E, Feng YT, Ranga K, Krishnan R: Neural network methods for volumetric magnetic resonance imaging of the human brain. *Proc IEEE* 84:1488–1496, 1996
22. Gelenbe E: Random neural networks with negative and positive signals and product form solution. *Neural Comput* 1(4):502–510, 1989
23. Gelenbe E: Stability of the random neural network model. *Neural Comput* 2(2):239–247, 1990
24. Gelenbe E: Learning in the recurrent random neural network. *Neural Comput* 5:154–164, 1993
25. Gelenbe E, Mao ZH, Li YD: Function approximation by random neural networks with a bounded number of layers. *J Differ Equ Dyn Syst* 12(1–2):143–170, 2004
26. Gelenbe E, Hussain K: Learning in the multiple class random neural network. *IEEE Trans Neural Netw* 13(6):1257–1267, 2002
27. Zadeh LA: Outline of a new approach to the analysis of complex systems and decision processes. *IEEE Trans Syst Man Cybern* 3:28–44, 1973
28. Zadeh LA: Knowledge representation in fuzzy logic. *IEEE Trans Knowl Data Eng* 1:89–100, 1989
29. Obuchowski NA, McClish DK: Sample size determination for diagnostic accuracy studies involving binomial ROC curve indices. *Statistics in Medicine* 16(13):1529–1542, 1997
30. Hanley JA, McNeil BJ: The meaning and use of the area under the receiver operation characteristic (ROC) curve. *Radiology* 143:29–36, 1982
31. Choi BC: Slopes of a receiver operating characteristic curve and likelihood ratios for a diagnostic test. *Am J Epidemiol* 148(11):1127–1132, 1998